MIT Open Access Articles

Magnetic nanopantograph in the SrCu[subscript 2] (BO[subscript 3])[subscript 2] Shastry-Sutherland lattice

Massachusetts Institute of Technology

Magnetic nanopantograph in the SrCu$_2$(BO$_3$)$_2$ Shastry–Sutherland lattice

Guillaume Radtke[a], Andrés Saúl[b,c,1], Hanna A. Dabkowska[d], Myron B. Salamon[e,f], and Marcelo Jaime[f]

[a]Institut de Minéralogie, de Physique des Matériaux et de Cosmochimie Sorbonne Universités—Université Pierre et Marie Curie Université Paris 06, UMR CNRS 7590, Muséum National d'Histoire Naturelle, Institut de Recherche pour le Développement UMR 206, F-75005 Paris, France; [b]Aix-Marseille University, Centre Interdisciplinaire de Nanoscience de Marseille-CNRS UMR 7325 Campus de Luminy, 13288 Marseille cedex 9, France; [c]Department of Civil and Environmental Engineering, Massachusetts Institute of Technology and MultiScale Material Science for Energy and Environment, UMI 3466 CNRS-MIT, Cambridge, MA 02139; [d]McMaster University, Brockhouse Institute for Materials Research, Hamilton, ON L8S 4M1, Canada; [e]Department of Physics, The University of Texas at Dallas, Richardson, TX 75080; and [f]National High Magnetic Field Laboratory, Los Alamos National Laboratory, Los Alamos, NM 87545

PHYSICS

Magnetic materials having competing, i.e., frustrated, interactions can display magnetism prolific in intricate structures, discrete jumps, plateaus, and exotic spin states with increasing applied magnetic fields. When the associated elastic energy cost is not too expensive, this high potential can be enhanced by the existence of an omnipresent magnetoelastic coupling. Here we report experimental and theoretical evidence of a nonnegligible magnetoelastic coupling in one of these fascinating materials, SrCu$_2$(BO$_3$)$_2$ (SCBO). First, using pulsed-field transversal and longitudinal magnetostriction measurements we show that its physical dimensions, indeed, mimic closely its unusually rich field-induced magnetism. Second, using density functional-based calculations we find that the driving force behind the magnetoelastic coupling is the $\widehat{CuOCu}$ superexchange angle that, due to the orthogonal Cu^{2+} dimers acting as pantographs, can shrink significantly (0.44%) with minute (0.01%) variations in the lattice parameters. With this original approach we also find a reduction of ~10% in the intradimer exchange integral J, enough to make predictions for the highly magnetized states and the effects of applied pressure on SCBO.

magnetostriction | high magnetic fields | spin-lattice coupling | density functional theory | Shastry–Sutherland

It has long been understood that magnetoelastic coupling can move magnetic materials phase boundaries in temperature and field and even change the order and/or universality class of magnetic transitions (1). Model Hamiltonians with effective exchange interactions are the common theoretical tool to tackle the complex behaviors of quantum magnet systems (2) and, indeed, these effective exchange interactions depend on subtleties of the electronic structure that, in turn, are naturally linked to the lattice degrees of freedom of the system. When magnetoelastic effects are present, structural changes can also modify the macroscopic magnetic state via changes in the effective parameters of the model Hamiltonian. Simply posed, it is challenging to interpret experimental results at a point of high interest in a predicted (H,T) phase diagram of a magnetic material under consideration for fundamental studies or applications without knowing the effects that unavoidable lattice changes have in the exchange interactions as we drive our system toward such a point. Hence, it is highly desirable to be able to quantify such lattice effects.

SrCu$_2$(BO$_3$)$_2$ (SCBO) is an especially fascinating example of a low-dimension, frustrated quantum antiferromagnetic system. It crystallizes in a tetragonal structure (3) in which layers of [CuBO$_3$]$^-$ (Fig. 1A) are stacked along the c axis and separated by planes of Sr^{2+} ions (Fig. 1B). The magnetically active Cu^{2+} ions form a 2D arrangement of mutually orthogonal dimers (Fig. 1A). The magnetic properties of this compound can be closely described through a 2D Heisenberg Hamiltonian (4):

$$H = J \sum_{nn} \mathbf{S}_i \cdot \mathbf{S}_j + J' \sum_{nnn} \mathbf{S}_i \cdot \mathbf{S}_j, \qquad [1]$$

where J and J' are respectively the nearest-neighbor (intradimer) and next-nearest-neighbor (interdimer) exchange integrals in the [CuBO$_3$]$^-$ planes. Although J and J' are both positive, leading to frustrated antiferromagnetic (AFM) interactions, Shastry and Sutherland (5) have shown the remarkable property that the Hamiltonian (Eq. 1) admits the direct product of dimer singlet states as an exact eigenstate. It has been first shown that this $S = 0$ wavefunction is the ground state for $J'/J \lesssim 0.7$, separated from the first excited state by a spin gap (4, 6, 7). More recently, the critical value has been refined to be $\simeq 0.675$ (8–10). The spin gap can be closed [the spin gap never strictly closes, as Dzyaloshinsky–Moriya terms cause mixing of spin-triplet and spin-singlet states (11)], and cascading magnetic states can be induced, by magnetic fields exceeding $\simeq 20$ T (12).

The first indications of a significant lattice involvement in this system were evidenced in the sound velocity measurements by Wolf et al. (13), subsequently studied using X-ray diffraction at low temperature and under high magnetic field by Narumi et al. (14). These were followed by neutron diffraction experiments carried out by Vecchini et al. (15) and Haravifard et al. (16). In the former, structural changes due to the thermal excitation of the magnetic degrees of freedom were directly measured. In the latter the increased lifetime (inelastic linewidths) in a subset of the acoustic phonons has been shown to correlate with the

Significance

The spins of the unpaired electrons in a solid tend to align along an applied magnetic field. In the case of antiferromagnetic materials having competing interactions (frustration) it is common to observe that the magnetization increases, exhibiting complicated structures with discrete jumps and plateaus. SrCu$_2$(BO$_3$)$_2$ is one of these materials, for which we find experimentally that its macroscopic physical dimensions also change with the magnetic field, mimicking the behavior in the magnetization. Using quantum mechanics, we show quantitatively that due to the orthogonal arrangement of the magnetic Cu^{2+} dimers acting as pantographs, minute deformations allow significant reduction in the effective interactions responsible for the antiferromagnetism. This drop is sufficient to compensate the elastic energy loss in the lattice deformation.
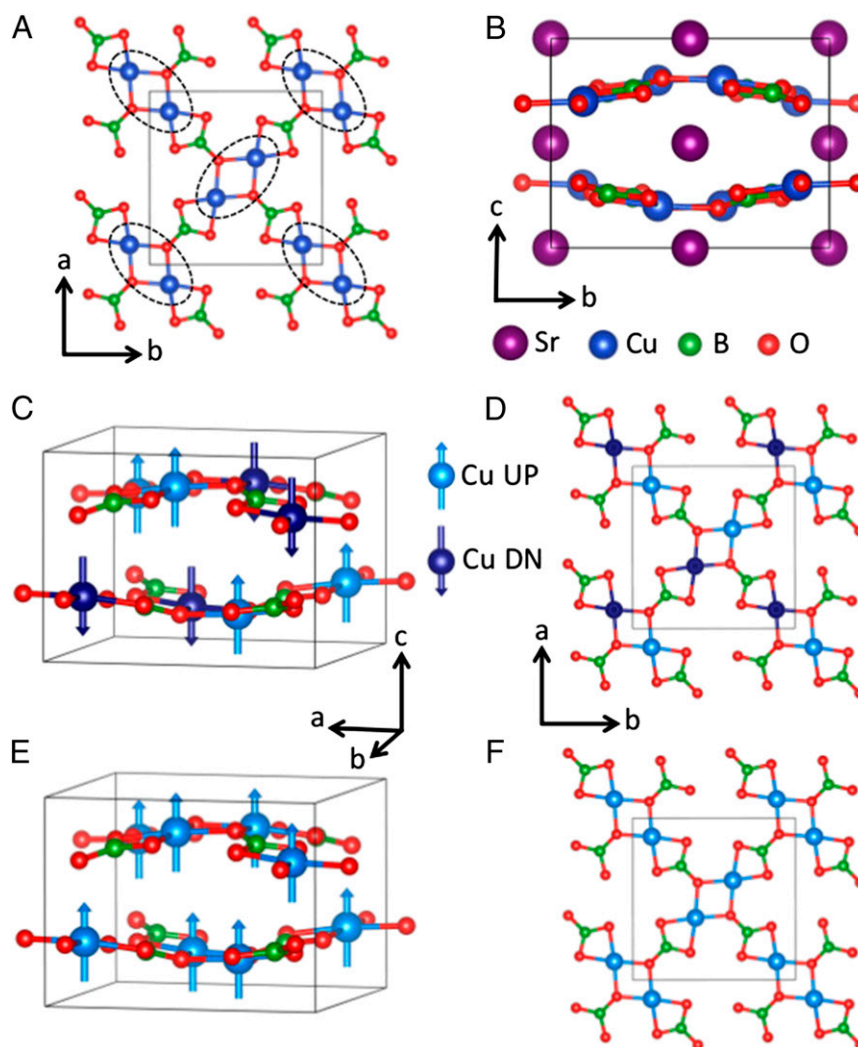
Fig. 1. Atomic structure and magnetic orders of $SrCu_2(BO_3)_2$. (*A*) Top view of the $[CuBO_3]^-$ layer. Sr^{2+} ions are omitted for clarity. Dashed ellipses emphasize structural dimers. (*B*) Side view of the tetragonal unit cell: Sr in magenta, O in red, B in green, and Cu in blue. The buckling of the $[CuBO_3]^-$ layers along the [001] direction is visible. (*C–F*) Néel-like AFM (*C* and *D*) and saturated FM (*E* and *F*) orders for DFT. Spin-up Cu ions are represented in light blue and spin-down Cu ions are represented in dark blue.

formation of the singlet ground state near 10 K in zero field. In a recent study, Jaime et al. (17) performed magnetostriction experiments to 100 T, showing that the crystallographic *c* axis is an extraordinarily sensitive witness to the magnetic structure and superstructure. However sensitive, the *c*-axis results do not allow for a direct examination of the spin-lattice correlations within the Cu-dimer planes (Fig. 1*A*).

Experimental Results

Using an experimental setup modified from one previously discussed (17), where an optical fiber Bragg grating (FBG) sensor is placed perpendicular to the applied magnetic field, we obtained the first high-resolution (better than 10^{-6}) in-plane magnetostriction at $T = 1.36$ K (Fig. 2). In our experiment we observe a contraction of the *a* axis that is sensitive to, and shows features at, the magnetic fields identified as onset of the 1/8, 1/4, and 1/3 magnetization plateaus and a concomitant expansion of the *c* axis with an FBG sensor in the conventional configuration parallel to the applied field. Our new data are consistent with *a*-axis vs. field data from Narumi et al. (14), although the X-ray experiment did not resolve individual plateaus. The observed

$\Delta a/a = -1.4 \times 10^{-4}$ and $\Delta c/c = 1.15 \times 10^{-4}$ put the relative change in volume at $\Delta V/V = -1.65 \times 10^{-4}$ for the 1/3 plateau.

Model

From a magnetic point of view, one can expect that the system will respond to the external magnetic field by modifying the internal coordinates of ions playing a role in the magnetic interactions. The modification of any other internal coordinates would have an elastic energy cost without magnetic energy gain. As already pointed out (14, 15), the main internal parameter related with the magnetic properties in this compound is the $\widehat{CuOCu}$ superexchange angle (α) mediating the intradimer superexchange interaction. This angle is, indeed, expected to decrease toward 90° with the applied magnetic field as this distortion would weaken the AFM superexchange interaction (18–21) through a reduction of the Cu-3*d*/O-2*p* hopping.

The orthogonal arrangement of the dimers in SCBO allows for a variation of the angle with a minimum lattice deformation. This double-pantograph (22) effect can be most easily visualized in Fig. 3 by considering the atoms moving as sketched. Each pantograph magnifies the decrease of the internal superexchange angles, but the two do not substantially change the overall length

Fig. 2. Magnetostriction vs. magnetic field. Shown is relative deformation $\Delta L/L$ along the tetragonal a and c crystallographic axis of SCBO vs. magnetic field applied along the c axis. Red curves are field upsweep, blue curves are field downsweep. Field hysteresis is likely due to magnetocaloric effect (17).

of the array. This argument can be demonstrated in a more rigorous way. Indeed, neglecting the buckling, the tetragonal unit cell parameter and the angle can be written as follows in terms of interatomic distances in the [CuBO$_3$]$^-$ layer (Fig. 3):

$$a \simeq \frac{1}{\sqrt{2}}\left[d_{\text{O–O}} + 2d_{\text{O–B}} + 2d_{\text{B–Cu}} + d_{\text{Cu–Cu}}\right] \qquad [2]$$

and

$$\tan\frac{\alpha}{2} \simeq \frac{d_{\text{Cu–Cu}}}{d_{\text{O–O}}}. \qquad [3]$$

Assuming that the O–B and B–Cu bonds are not affected by the magnetic field, and calling x the O–O and y the Cu–Cu distances, their variations can be written as

$$\Delta a = \frac{1}{\sqrt{2}}(\Delta x + \Delta y) \qquad [4]$$

and

$$\Delta\alpha = \frac{2\,x\,y}{x^2+y^2}\left[\frac{\Delta y}{y} - \frac{\Delta x}{x}\right]. \qquad [5]$$

Under an increasing magnetic field, the system can reduce the magnetic contribution to the total energy by decreasing the superexchange angle ($\Delta\alpha < 0$) through an increase of the O–O distance ($\Delta x > 0$) or a decrease of the Cu–Cu one ($\Delta y < 0$). Because the variation in the Cu–Cu distance compensates the variation in the O–O distance $\Delta x \sim -\Delta y$, it follows that $\Delta a/a \ll \Delta\alpha$. The magnetic energy gain from the increase in antiferromagnetic exchange is not, therefore, at the expense of a significant increase in lattice energy.

Theoretical Results

Structure Relaxation—Angle.
To gain insight into the modification of the internal structural parameters and their consequences on the electronic structure and magnetic interactions with a change of the magnetic order, total energy calculations have been performed with the Quantum Espresso (23) code.

As, in our problem, magnetostriction involves only very weak structural variations, it would be of interest to compare the

structural relaxation of two extreme magnetic states, namely the ground state configuration (a product of dimer singlets) and the ferromagnetic (FM) state expected at saturation. Unfortunately, the ground state solution cannot be written as a single Kohn–Sham determinant and is therefore not accessible with state-of-the-art density functional theory (DFT) codes for periodic systems. For this reason, we have optimized the lattice parameters and internal atomic coordinates of a Néel-like AFM ordered structure and of the FM state (Fig. 1 C–F). Using the Quantum Espresso code (23), we obtained lattice parameters ($a = 9.123$ Å and $c = 6.853$ Å) that are slightly overestimated as is usually the case with the generalized gradient approximation of Perdew, Burke, and Ernzerhof (GGA-PBE) functional. As expected from the above discussion, due to the (Δx, Δy) compensation effect, no measurable difference between the lattice parameters of the AFM and FM ordered structures was found. The order of magnitude of their relative difference (experimentally found to be $\simeq 10^{-4}$) indeed falls within the limit of accuracy of DFT when trying to calculate the structural changes between two magnetic orders with different space symmetries.

The difference in α and the O–O and Cu–Cu distances (respectively x and y) between the two magnetic structures are more easy to assess with DFT. A variation of the angle of $\Delta\alpha = -0.43°$ (98.13° and 97.70° for the AFM and FM structures, respectively) has been found whereas the O–O and Cu–Cu distance changes are $\Delta x = 0.011$ Å and $\Delta y = -0.009$ Å, respectively. As already mentioned, their relative variations ($\Delta x/x \simeq 44 \times 10^{-4}$ and $\Delta y/y \simeq -31 \times 10^{-4}$) are larger than the variation of $\Delta a/a$.

Effective Exchange Interactions from Energy Differences.
The computation of magnetic couplings was first carried out within the broken symmetry formalism, i.e., by mapping total energies corresponding to various collinear spin arrangements within a supercell onto a Heisenberg Hamiltonian,

$$\hat{H} = \hat{H}_0 + \sum_{i>j} J_{ij}\,\hat{\mathbf{S}}_i \cdot \hat{\mathbf{S}}_j, \qquad [6]$$

where $\hat{H}_0$ is the spin-independent part of the Hamiltonian, J_{ij} are the magnetic couplings to determine, and $\hat{\mathbf{S}}_i$ and $\hat{\mathbf{S}}_j$ are, in our case, the $S = 1/2$ spin operators localized on Cu^{2+} ions located at sites i and j, respectively. It is straightforward to show that the expectation value of the Hamiltonian (6) on a DFT state $|\alpha\rangle$ (obtained by preparing the initial electron density according to

Fig. 3. Schematic representation of the pantograph mechanism. It allows a modification of the $\overline{\text{CuOCu}}$ superexchange angle with an $\sim$35× reduced effect (main text) on the lattice parameter. O atoms are in red, B in green, and Cu in blue.

a particular collinear spin arrangement in the supercell and performing a self-consistent calculation until convergence) can be simply written under the form of an Ising Hamiltonian (24)

$$\epsilon_\alpha^{\text{DFT}} = \langle \alpha | \hat{H} | \alpha \rangle = \epsilon_0 + \frac{1}{4} \sum_{i>j} J_{ij} \sigma_i \sigma_j \qquad [7]$$

with $\sigma_i = \pm 1$. It is important to note that this broken symmetry procedure preserves the quantum nature of the problem. In strongly localized systems, such as $3d$ transition metal oxides, Eq. 7 can be used to model a large set of spin configurations. A numerical evaluation of the couplings is thus obtained through a least-squares minimization of the difference between DFT and Ising relative energies of the set of spin configurations (25–27).

In the case of SCBO the determination of the magnetic couplings up to the fifth nearest neighbor (in the 3D lattice) can be performed using a 44-atom tetragonal cell. Taking crystal and spin reversal symmetries into account, this leads to a total of 22 distinct spin configurations. The calculations using the internal parameters of the relaxed AFM and FM ordered structures give $J = 157$ K and $J = 138$ K, respectively. A reduction of the in-plane nearest-neighbor interaction of $\sim -12\%$ is therefore obtained, in agreement with the decrease of the angle. On the contrary, the in-plane second-nearest-neighbor interaction remains the same $J' = 71$ K in both cases. Additional calculated couplings correspond to interplan couplings. They are all antiferromagnetic and show a much weaker amplitude (≤ 4 K), independent of the set of internal coordinates employed in the calculations. The results of the mapping procedure are shown in Fig. 4.

Effective Exchange Interactions from Band Structure–Wannier Functions. An alternative evaluation of the AFM contribution to the magnetic couplings can be achieved through a mapping of the paramagnetic band structure onto a single-band Hubbard model at half filling, which eventually reduces to an Heisenberg model in the strongly correlated limit. In this framework, the effective antiferromagnetic interaction is given by $J^{\text{afm}} = 4t^2/U$.

Fig. 4. Comparison of the optimized energies calculated with the Ising Hamiltonian vs. the DFT + U calculated ones. Shown is a graphical representation of the results obtained by using the least-squares fit procedure for internal coordinates optimized with both FM and AFM magnetic orders: For each spin configuration, the DFT + U relative energy is represented as a function of the optimized Ising energy. Positive couplings correspond to AFM interactions.

The Wannier-interpolated band structure obtained following this procedure is superimposed to the GGA-PBE band structure in Fig. 5. Fig. 5, *Inset* shows the maximally localized Wannier functions (MLWF) calculated for the FM internal coordinates. Besides the central Cu-$d_{x^2-y^2}$ component, large antibonding tails of O-$2p$ character mediating the dominant in-plane superexchange antiferromagnetic interactions are also clearly visible. Note that a MLWF calculated for the AFM internal coordinates would be indistinguishable at this scale. The hopping integrals t and t' corresponding to the first and second effective exchange interactions are 0.153 eV and −0.096 eV for the AFM internal coordinates and 0.148 eV and −0.096 eV for the FM ones.

There is a small but measurable decrease of the nearest-neighbors hopping interaction t but no difference in the next-nearest-neighbors interaction t'. The different behavior can be ascribed to the decrease of the intradimer $\widehat{\text{CuOCu}}$ superexchange angle contrasting with the above mentioned rigidity of the BO$_3$ group. The variation of the nearest-neighbors effective exchange interaction estimated through this approach is $\Delta J^{\text{afm}}/J^{\text{afm}} = -6.5\%$, i.e., of the same order of magnitude as the modification estimated with the broken symmetry formalism. The difference is likely to arise from the fact that this procedure gives only the antiferromagnetic contribution to the total effective exchange interaction missing a known nonnegligible ferromagnetic component (28).

Discussion

It is possible to establish a relation between the intradimer $\widehat{\text{CuOCu}}$ superexchange angle and the subsequent lattice parameter variations based on a simple geometrical interpretation of the structural data available on this compound. We should first eliminate Δx in Eqs. 4 and 5 to obtain

$$\Delta \alpha = \frac{2(x+y)}{x^2+y^2} \Delta y - \frac{2\sqrt{2}y}{x^2+y^2} \Delta a. \qquad [8]$$

To further eliminate Δy, we can consider that the structural variations induced by thermal excitation of the dimer singlets are equivalent to the variations obtained by application of an external magnetic field. Under this assumption, a linear dependence $\Delta \alpha = k\, \Delta y$ with $k = 36.6 \pm 0.8°\,\text{Å}^{-1} = 0.64 \pm 0.01\,\text{Å}^{-1}$ (Fig. S1) can be deduced from temperature-dependent neutron diffraction experiments (15) to obtain

$$\Delta \alpha = \frac{2\sqrt{2}ky}{2(x+y) - k(x^2+y^2)} \Delta a. \qquad [9]$$

Similar functions of x, y, and k can be obtained for Δx, Δy, and Δd the Cu–O distance (*SI Text*). Finally, replacing x, y, and a by their experimental values (15), we obtain

$$\Delta \alpha \simeq 35\,\frac{\Delta a}{a}, \quad \frac{\Delta x}{x} \simeq -17\,\frac{\Delta a}{a}, \quad \frac{\Delta y}{y} \simeq 19\,\frac{\Delta a}{a}, \qquad [10]$$

showing that the deformation of the lattice parameter can be related to one order of magnitude larger variations of the internal parameters. Indeed, the experimentally measured low temperature magnetostriction at 60 T is 1.15×10^{-4} and -1.4×10^{-4} along the c and a axes, respectively. These changes imply a drop in α of 0.28° and relative variations $\Delta x/x \simeq 24 \times 10^{-4}$ and $\Delta y/y \simeq -26 \times 10^{-4}$. Furthermore, one should expect that magnetostriction to 100 T along the c axis of 1.6×10^{-4} (17) would be accompanied by magnetostriction of 1.95×10^{-4} along the a axis and a change in α of 0.40°, altogether in remarkable agreement with our DFT results, confirming that α is the driving mechanism behind the magnetoelastic coupling in SCBO.

Coming back to DFT calculations, we can now confirm that the energetic arguments used to justify the pantograph effect are
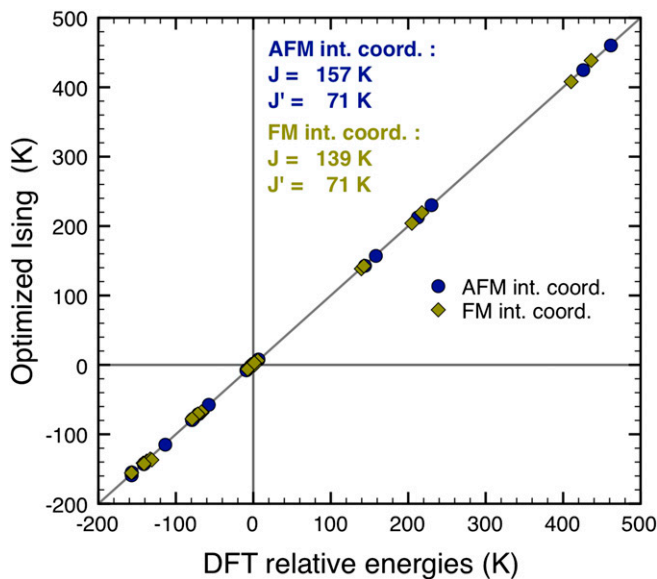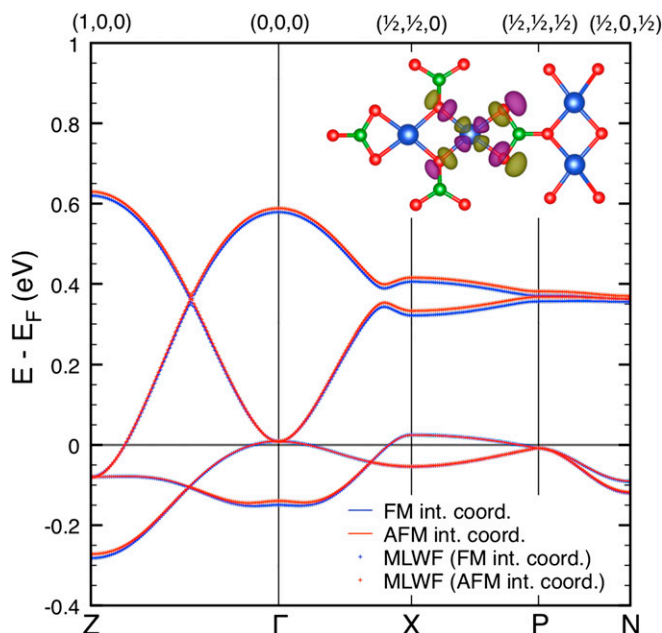
Fig. 5. Comparison of the band structures calculated for AFM and FM internal coordinates. Shown is nonmagnetic GGA-PBE band structure close to the Fermi level of SCBO calculated for both FM (blue) and AFM (red) magnetic configurations. The high-symmetry point coordinates in the Brillouin zone are given in units of the reciprocal lattice basis vectors of the tetragonal unit cell. *Inset* shows MLWF centered on a Cu site calculated using the internal coordinates obtained for a FM order. Large antibonding O-2p tails are clearly visible.

correct. Indeed, from the variation of J for a tetragonal unit cell, we can estimate the magnetic energy gain due to the magnetoelastic coupling to be about -10 K or $\Delta E_H \simeq -8 \times 10^{-4}$ eV/unit cell. Also, from the experimental deformations and calculated elastic constants, the elastic energy loss due to the magnetostriction can be estimated to be about $\Delta E_{\text{elast}} \simeq 7 \times 10^{-5}$ eV/unit cell, one order of magnitude smaller than the magnetic energy (*Materials and Methods*).

Moreover, our calculations predict a strong effect ($\sim$10% reduction) in the intradimer exchange integral J as α decreases, with no detectable variation in the interdimer counterpart J'. These results have implications in the reading of phase diagrams such as (H/J, J'/J) discussed by Matsuda et al. (29). As the J'/J ratio increases with the applied magnetic field, the high-field part of the phase diagram should be read following a diagonal line oriented to the right. Indeed, the absence of the 2/5 plateau reported in the magnetization vs. field experiments in ref. 29 or the small stability region observed in the magnetostriction experiments in ref. 17 can be explained as being due to an increase of the exchange interaction ratio J'/J in the high-field region.

Our results could also shed light on 2D models used so far to predict magnetization plateaus, as the expected changes in $\widehat{\text{CuOCu}}$ angle and J can have different effects on different models and help to sort them out according to prediction power. As we show, the reduction in J comes alongside a drop in the volume of the crystallographic unit cell of SCBO that is usually the effect of applied pressures. In simpler words, our results also suggest that pressures of the order of a few gigapascals might be used to control the J'/J parameter through the pantograph effect and therefore to drive SCBO out of the spin dimer ground state into plaquette or Néel order. Magnetic susceptibility vs. pressure and very recent neutron diffraction under pressure results (30, 31) support these ideas. We also note that low temperature active Raman modes have been identified as being correlated with the spin gap in $SrCu_2(BO_3)_2$

(32). Among these, the Q^{IA_1} optical mode discussed by Choi et al. (33) is of special interest as its symmetry is compatible with the pantograph effect discussed here.

In summary, our original approach and results shed light on the issue of tuning magnetic ground states of matter with the use of external magnetic fields and pressure, by means of a clever combination of state-of-the-art experimental and computational tools.

Materials and Methods

Experimental. The high-quality single-crystal samples used in this work were prepared by the optical floating zone image furnace technique using self-flux as described elsewhere (34), oriented, and cut into $\sim$2 $\times$ 2 $\times$ 3-mm^3 pieces for the magnetostriction experiment. Magnetostriction measurements were carried out using an optical fiber, furnished with a FBG, attached to the sample to detect length variations as a rapidly varying external magnetic field is applied (17). The reflection of light by the FBG at the Bragg wavelength shifts when the grating spacing changes. In our experimental setup, two different configurations were used to measure in-plane and out-of-plane magnetostriction. In the latter case, $\Delta c/c$ is measured with the fiber and magnetic field both along the crystallographic c axis whereas in the former case, the fiber is bent around a circle of 0.6-inch diameter and kept in place with a stainless steel fine diameter tube to reach the sample at 90° from the c axis (and magnetic field H) and thus obtain $\Delta a/a$.

Computational. Total energy calculations were performed with the Quantum Espresso (23) code. This code is based on DFT and uses the pseudopotential plane-wave method. The calculations were performed using ultrasoft pseudopotentials (35). For exchange and correlation, we used the GGA-PBE (36) augmented by a Hubbard U term to improve the treatment of strongly correlated Cu-3d electrons. A value of the effective Hubbard $U = 10.3$ eV was determined in a 44-atom tetragonal cell, using the experimental structure determined at 300 K (3) with a ferromagnetic order and following the approach proposed in ref. 37. For structural relaxations, a plane-wave cutoff of 60 Ry and a 6 $\times$ 6 $\times$ 6 Monkhorst–Pack (38) grid for the first Brillouin zone sampling were used. At the end of the relaxation procedure the total pressures were lower than 0.35 kbar and the forces were less than 10^{-4} Ry/bohr.

The mapping of the paramagnetic band structure onto a single-band Hubbard model at half filling was performed first by computing a set of four maximally localized Wannier functions following the method of Marzari and Vanderbilt (39) and spanning the four bands of dominant Cu-$d_{x^2-y^2}$ character located between -0.4 eV and 0.65 eV. Maximally Localized Wannier Function interpolation of the band structure was calculated using Wannier90 (40) interfaced with Quantum Espresso.

To check the hypothesis that the lattice distortion is fairly inexpensive in SCBO, due to the opposing pantographs in the crystallographic unit cell, we compute the energy involved in the magnetostriction at saturation (ferromagnetic order). If we consider that the total energy of the system can be decomposed in Zeeman, Heisenberg, and elastic contributions, the energy difference between the deformed and undeformed systems can be compared. First, one can suppose that the Zeeman term does not depend on the deformation. Second, for a tetragonal unit cell the energy gain due to the magnetostriction is $\Delta E_H \simeq \Delta J + 4\Delta J'$, which can be estimated to be about -10 K or $\Delta E_H \simeq -8 \times 10^{-4}$ eV/unit cell. Finally, for a tetragonal deformation, the elastic contribution can be calculated as

$$\Delta E_{\text{elast}} = V\left[(c_{11}+c_{12})\,\epsilon_a^2 + \frac{1}{2}\,c_{33}\,\epsilon_c^2 + 2\,c_{13}\,\epsilon_c\epsilon_a\right], \qquad [11]$$

where $V = a^2c$ is the volume; $\epsilon_a \simeq -2 \times 10^{-4}$ and $\epsilon_c \simeq 2 \times 10^{-4}$ are the extrapolated in-plane and out-of-plane deformations; and $c_{11} = 36.9 \times 10^{11}$, $c_{12} = 13.2 \times 10^{11}$, $c_{33} = 6.7 \times 10^{11}$, and $c_{13} = 2.3 \times 10^{11}$ erg/cm^3 are the elastic constants of SCBO calculated with Quantum Espresso (23) in GGA + U for the FM unit cell. The elastic energy loss is then $\Delta E_{\text{elast}} \simeq 7 \times 10^{-5}$ eV/unit cell.

1. Boubcheur EH, Massimino P, Diep HT (2001) Effects of magnetoelastic coupling: Critical behavior and structure deformation. *J Magn Magn Mater* 223(2):163–168.
2. Zapf V, Jaime M, Batista CD (2014) Bose-Einstein condensation in quantum magnets. *Rev Mod Phys* 86(2):563–614.
3. Smith RW, Kesler DA (1991) Synthesis, structure, and properties of the orthoborate $SrCu_2(BO_3)_2$. *J Solid State Chem* 93(2):430–435.
4. Miyahara S, Ueda K (1999) Exact dimer ground state of the two dimensional Heisenberg spin system $SrCu_2(BO_3)_2$. *Phys Rev Lett* 82(18):3701–3704.
5. Shastry BS, Sutherland B (1981) Exact ground state of a quantum mechanical antiferromagnet. *Physica B* 108(1-3):1069–1070.
6. Weihong Z, Hamer CJ, Oitmaa J (1999) Series expansions for a Heisenberg antiferromagnetic model for $SrCu_2(BO_3)_2$. *Phys Rev B* 60(9):6608–6616.
7. Koga A, Kawakami N (2000) Quantum phase transitions in the Shastry-Sutherland model for $SrCu_2(BO_3)_2$. *Phys Rev Lett* 71(4):092403.
8. Müller-Hartmann E, Singh RRP, Knetter C, Uhrig GS (2000) Exact demonstration of magnetization plateaus and first-order dimer-Neel phase transitions in a modified Shastry-Sutherland model for $SrCu_2(BO_3)_2$. *Phys Rev Lett* 84(8):1808–1811.
9. Darradi R, Richter J, Farnell DJJ (2005) Coupled cluster treatment of the Shastry-Sutherland antiferromagnet. *Phys Rev B* 72(10):104425.
10. Corboz P, Mila F (2013) Tensor network study of the Shastry-Sutherland model in zero magnetic field. *Phys Rev B* 87(11):115144.
11. Jorge GA, et al. (2005) Crystal symmetry and high-magnetic-field specific heat of $SrCu_2(BO_3)_2$. *Phys Rev B* 71(9):092403.
12. Kageyama H, et al. (1999) Exact dimer ground state and quantized magnetization plateaus in the two-dimemssion spin system $SrCu_2(BO_3)_2$. *Phys Rev Lett* 82(15): 3168–3171.
13. Wolf B, et al. (2001) Soft acoustic modes in the two-dimensional spin system $SrCu_2(BO_3)_2$. *Phys Rev Lett* 86(21):4847–4850.
14. Narumi Y, et al. (2009) Field induced lattice deformation in the quantum antiferromagnet $SrCu_2(BO_3)_2$. *J Phys Soc Jpn* 78(4):043702.
15. Vecchini C, et al. (2009) Structural distortions in the spin-gap regime of the quantum antiferromagnet $SrCu_2(BO_3)_2$. *J Solid State Chem* 82(12):3275–3281.
16. Haravifard S, Gaulin BD, Yamani Z, Dunsiger SR, Dabkowska HA (2012) Neutron scattering from the static and dynamic lattice of $SrCu_2(BO_3)_2$ in its Shastry-Sutherland singlet ground state. *Phys Rev B* 85(13):134104.
17. Jaime M, et al. (2012) Magnetostriction and magnetic texture to 100.75 Tesla in frustrated $SrCu_2(BO_3)_2$. *Proc Natl Acad Sci USA* 109(31):12404–12407.
18. Goodenough JB (1955) Theory of the role of covalence in the perovskite-type manganites [La, M(II)]MnO₃. *Phys Rev* 100(2):564–573.
19. Goodenough JB (1958) An interpretation of the magnetic properties of the perovskite-type mixed crystals $La_{1-x}Sr_xCoO_{3-\lambda}$. *J Phys Chem Solids* 6(2-3):287–297.
20. Kanamori J (1959) Superexchange interaction and symmetry properties of electron orbitals. *J Phys Chem Solids* 10(2-3):87–98.
21. Anderson PW (1959) New approach to the theory of superexchange interactions. *Phys Rev* 115(1):2–13.
22. Scheiner C (1631) *Pantographice seu Ars Delineandi Res Quaslibet Per Parallelogrammum Lineare Seu Cavum* (Ex typographia Ludouici Grignani, Rome). Latin.
23. Giannozzi P, et al. (2009) QUANTUM ESPRESSO: A modular and open-source software project for quantum simulations of materials. *J Phys Condens Matter* 21(39):395502.
24. Radtke G, Saúl A, Dabkowska HA, Luke GM, Botton GA (2010) Interplay between structural, electronic, and magnetic degrees of freedom in $Sr_3Cr_2O_8$. *Phys Rev Lett* 105(3):036401.
25. Saúl A, Radtke G (2011) Magnetic couplings in CsV_2O_5: A new picture. *Phys Rev Lett* 106(17):177203.
26. Saúl A, Vodenicarevic D, Radtke G (2013) Theoretical study of the magnetic order in α-CoV_2O_6. *Phys Rev B* 87(2):024403.
27. Saúl A, Radtke G (2014) Density functional approach for the magnetism of β-$TeVO_4$. *Phys Rev B* 89(10):104414.
28. Mazurenko VV, Skornyakov SL, Anisimov VI, Mila F (2008) First-principles investigation of symmetric and antisymmetric exchange interactions of $SrCu_2(BO_3)_2$. *Phys Rev B* 78(19): 195110.
29. Matsuda YH, et al. (2013) Magnetization of $SrCu_2(BO_3)_2$ in ultrahigh magnetic fields up to 118 T. *Phys Rev Lett* 111(13):137204.
30. Kageyama H, Mushnikov NV, Yamada M, Goto T, Ueda Y (2003) Quantum phase transitions in the orthogonal dimer system $SrCu_2(BO_3)_2$. *Physica B* 329–333:1020–1023.
31. Haravifard S, et al. (2014) Emergence of long-range order in sheets of magnetic dimers. *Proc Natl Acad Sci USA* 111(40):14372–14377.
32. Lemmens P, et al. (2000) Collective singlet excitations and evolution of raman spectral weights in the 2D spin dimer compound $SrCu_2(BO_3)_2$. *Phys Rev Lett* 85(12): 2605–2608.
33. Choi KY, et al. (2003) Strong anharmonicity and spin-phonon coupling in the quasi-two-dimensional quantum spin system $Sr_{1-x}Ba_xCu_2(BO_3)_2$. *Phys Rev B* 68(10):104418.
34. Dabkowska HA, et al. (2007) Crystal growth and magnetic behaviour of pure and doped $SrCu_2(BO_3)_2$. *J Cryst Growth* 306(1):123–128.
35. Garrity KF, Bennett JW, Rabe KM, Vanderbilt D (2014) Pseudopotentials for high-throughput DFT calculations. *Comput Mater Sci* 81:446–452.
36. Perdew JP, Burke K, Ernzerhof M (1996) Generalized gradient approximation made simple. *Phys Rev Lett* 77(18):3865–3868.
37. Cococcioni M, de Gironcoli S (2005) Linear response approach to the calculation of the effective interaction parameters in the LDA+U method. *Phys Rev B* 71(3):035105.
38. Monkhorst HJ, Pack JD (1976) Special points for Brillouin-zone integrations. *Phys Rev B* 13(12):5188–5192.
39. Marzari N, Vanderbilt D (1997) Maximally localized generalized Wannier functions for composite energy bands. *Phys Rev B* 56(20):12847–12865.
40. Mostofi AA, et al. (2008) Wannier90: A tool for obtaining maximally-localised Wannier functions. *Comput Phys Commun* 178(9):685–699.